CrossMark

Numerical Convergence of 2D Solar Convection in Implicit Large-eddy Simulations

H. D. Nogueira[1,2], G. Guerrero[1,3] , P. K. Smolarkiewicz[4], and A. G. Kosovichev[3]

[1] Physics Department, Universidade Federal de Minas Gerais, Avenida Antonio Carlos, 6627, Belo Horizonte, MG 31270-901, Brazil; guerrero@fisica.ufmg.br
[2] Laboratoire Kastler Brossel, Sorbonne Université, CNRS, ENS-Université PSL, Collège de France, 4 place Jussieu, F-75005 Paris, France
[3] New Jersey Institute of Technology, Newark, NJ 07103, USA
[4] National Center for Atmospheric Research, Boulder, CO 80305, USA

Abstract

Large-eddy simulations (LES) and implicit LES (ILES) are wise and affordable alternatives to the unfeasible direct numerical simulations of turbulent flows at high Reynolds (Re) numbers. However, for systems with few observational constraints, it is a formidable challenge to determine if these strategies adequately capture the physics of the system. Here, we address this problem by analyzing numerical convergence of ILES of turbulent convection in 2D, with resolutions between 64^2 and 2048^2 grid points, along with the estimation of their effective viscosities, resulting in effective Reynolds numbers between 1 and $\sim 10^4$. The thermodynamic structure of our model resembles the solar interior, including a fraction of the radiative zone and the convection zone. In the convective layer, the ILES solutions converge for the simulations with $\geqslant 512^2$ grid points, as evidenced by the integral properties of the flow and its power spectra. Most importantly, we found that even a resolution of 128^2 grid points, Re ~ 10, is sufficient to capture the dynamics of the large scales accurately. This is a consequence of the ILES method allowing the energy contained in these scales to be the same in simulations with low and high resolution. Special attention is needed in regions with a small density scale height driving the formation of fine structures unresolved by the numerical grid. In the stable layer, we found the excitation of internal gravity waves, yet high resolution is needed to capture their development and interaction.

Unified Astronomy Thesaurus concepts: Solar convective zone (1998); Hydrodynamical simulations (767); Computational methods (1965)

Supporting material: animations

1. Introduction

Turbulent convection is ubiquitous in astrophysics and geophysics, taking place in planetary atmospheres and oceans, and inside stars. It is a nonlinear problem for which analytic solutions are scarce and limited in scope. On the other hand, laboratory experiments are able to explore only a fraction of the parameter space spanned by convection in nature. Thus, many scientists turn to computer simulations to investigate this phenomenon. The simulations are carried out for ideal situations, such as Rayleigh–Bénard convection (Sakievich et al. 2016; Stevens et al. 2018), as well as for several cases observed in nature ranging from stellar convection (e.g., Elliott & Smolarkiewicz 2002; Brandenburg et al. 2005; Guerrero et al. 2016a, 2016b; Featherstone & Hindman 2016; Kitiashvili et al. 2016; Käpylä et al. 2019) to the Earth's and planetary atmospheres as well as oceans and mantle currents (Ganot et al. 2014; Peña-Ortiz et al. 2019; Wang et al. 2019).

A simulation resolving all the relevant scales of the flow is called direct numerical simulation (DNS). In DNS, the resolved scales range from the largest scale to the smallest Komolgorov scale, at which dissipation occurs. In high Reynolds number systems, such as in the solar convection zone, the ratio between the largest and the smallest scales is extremely large. Consequently, to capture all relevant scales, the domain discretization must be excessively fine ($N^D \sim \text{Re}^{3D/4}$, where N is the number of grid points, and D is the number of spatial

dimensions, Pope 2011). These simulations are still unfeasible for modern supercomputers. The expectation is that with progressively increasing the resolution the prognostic variables reach an asymptotic regime of convergent values for $N^D \ll \text{Re}^{3D/4}$. This would mean that the relevant scales for a given system are larger than the Kolmogorov scale, and that the dissipative processes are governed by turbulence. For instance, the reality of the concept of turbulent viscosity for solar convection was proposed by Schwarzschild (1959) to explain the first observations of solar granulation, arguing that the Reynolds number of these motions must be $\mathcal{O}(1)$ (see also Canuto 2000; Stothers 2000).

Of course, dissipation is not the only contribution of turbulence, which poses a problem for DNS. Given the restricted numerical resolution, suitable values for the dissipation coefficients, i.e., dynamic viscosity (ν), heat conduction (κ), or magnetic diffusivity (η), in hydrodynamic and magnetohydrodynamic simulations of convection, are typically orders of magnitude larger than the theoretical estimations of collisional transport coefficient in gas and plasma. Even though in DNS the explicit values of these parameters approach those estimated for turbulent dissipation coefficients, the results do not seem to achieve this asymptotic regime. For instance, Featherstone & Hindman (2016) performed DNS of solar convection in spherical shells progressively increasing the Rayleigh (Ra) number. While they found that the energy becomes independent of the heat conduction after a certain value of the Rayleigh number Ra, neither the spectral distribution of energy nor the radial profile of the vertical velocity indicated numerical convergence. In other words, it is

unknown to what extent the numerical models of this phenomenon represent reality.

An alternative to DNS is the large-eddy simulation approach (LES). In LES, all the scales down to the numerical cutoff scale are simulated, while the action of unresolved scales is parameterized using the simulated values and turbulence scaling laws. It is a well-founded assumption as to when the unresolved turbulent flow is scale invariant. However, this condition is not entirely fulfilled in convective systems with strong density stratification, rotation and/or other factors making the motions anisotropic (Elliott & Smolarkiewicz 2002). By using implicit large-eddy simulations (ILES), the contribution of the unresolved scales can be modeled by specially designed finite-difference truncation terms of the numerical advection. In the ILES methodology, these terms act as an effective dissipation, e.g., effective viscosity for the transport of momentum, and as an energy flux between scales (Margolin & Rider 2002).

The numerical convergence of ILES simulations is not easy to define. Since the terms in ILES would be truncated at a different scale, changing the spatial resolution of the simulation would necessarily affect the results. Thus, the numerical convergence in such a situation is scale dependent as for increasing numerical resolution the large-scale properties of the flow remain unaltered while more and more small-scale structures develop. Therefore, in this respect, the ILES approach is different from the LES, and requires a detailed investigation of the numerical convergence for particular classes of models.

This study explores the numerical convergence in ILES 2D simulations of turbulent stratified convection, which mimics the solar convection zone. We do not aim to compare the results to any particular analytical solution or observations of a physical system, but explore whether the integral characteristics of a numerical model reach a converged state when the resolution increases. The initial and boundary conditions of our model resembles the solar convection zone, turbulent characteristics of which are still uncertain and currently debated (Greer et al. 2015; Hanasoge et al. 2016). In this work numerical convergence will be evaluated in terms of the vertical profiles of temporally and horizontally averaged quantities, like the turbulent velocities and the convective heat flux. The distribution of energy along the different spatial scales resolved for each grid is assessed through the turbulent spectra of the kinetic energy and the variance of potential temperature. An approximated analysis of the effects of the ILES method on the dynamics of the system is performed from the estimation of an effective viscosity as a function of the scale. We compare this quantity with the turbulent viscosity, which is a rough measure of the enhancement of transport of momentum and other physical quantities by turbulence. It is computed here from the length and timescales of the most energetic motions. Finally, the unexpected development of oscillatory mean horizontal motions in the stable layer will also be presented.

A similar convergence study was performed by Porter & Woodward (1994), who used the ILES scheme based on a piecewise parabolic method (PPM; Colella & Woodward 1984), devoid of explicit viscosity in the momentum equation, and reached resolutions up to 1024×256 grid points (corresponding to Re $\sim 2 \times 10^4$). They found that at lower resolutions the vertical size of the convection cells occupy the entire convection zone. For the highest resolution models, the small eddies break down the large cells resulting in a flow dominated by structures of all sizes but without large-scale convection cells. In the 3D simulations, they modified the upper thermal boundary condition allowing for the temperature to be constant in space but change with time (Porter & Woodward 2000). They observed convergence in the results for their high-resolution cases. Sullivan & Patton (2011) presented a convergence analysis for 3D LES simulations of the Earth's convective boundary layer. They found that numerical convergence is achieved whenever there is enough scale separation between the most energetic eddies and those with scales close to the cutoff of the LES scheme. Besides the global convection simulations of Featherstone & Hindman (2016) described above, to our knowledge DNS of stratified turbulent convection has not explored the role of resolution.

Three-dimensional simulations provide a better representation of the convection zone dynamics. For instance, in the presence of rotation and magnetic fields, the collective 3D effects of turbulence include the generation of large-scale flows and dynamos. Most of these effects either do not exist or take a different form in 2D convection. Nevertheless, the influence of the finest scales on the largest scales is worth exploring, as it sheds light on turbulent convection as well as on the capabilities of ILES. In this work, we focus on 2D convection, which allows for higher resolutions, while leaving 3D simulations for future studies.

This paper is organized as follows. In Section 2, we describe the equations, the numerical model, and other ingredients used to simulate turbulent convection. In Section 3, we perform the convergence analysis by varying the numerical resolution. Finally, in Section 4, we present our concluding remarks.

2. Numerical Model

We used the EULAG-MHD code (Smolarkiewicz & Charbonneau 2013)—a specialized variant of the original EULAG code (Prusa et al. 2008)—to perform two-dimensional convection simulations in a rectangular domain. EULAG-MHD is based on the multidimensional positive-definite advection transport algorithm, MPDATA (Smolarkiewicz 2006). It is a non-oscillatory forward-in-time advection solver with second-order accuracy in space and time. The code allows simulations to be run as ILES without any explicit dissipation (note that it also may be used for DNS with explicit dissipation). In the current model setup the vertical coordinate, z, spans from 0–$L_z = 254$ Mm (covering most of the depth of the solar convection zone and upper layers of the radiative zone), while the horizontal coordinate, x, spans from 0 –$L_x = 2.5L_z$. The number of grid points is the same in the vertical and horizontal directions in each simulation. We solved the following set of Navier–Stokes equations governing mass, momentum, and energy conservation:

$$\nabla \cdot \rho_r \boldsymbol{u} = 0, \qquad (1)$$

$$\frac{d\boldsymbol{u}}{dt} = -\nabla \pi' - \boldsymbol{g} \frac{\Theta'}{\Theta_r}, \qquad (2)$$

$$\frac{d\Theta'}{dt} = -\boldsymbol{u} \cdot \nabla \Theta_a - \alpha \Theta', \qquad (3)$$

where $d/dt = \partial/\partial t + \boldsymbol{u} \cdot \nabla$, $\boldsymbol{u}$ is the velocity field, ρ_r is the reference state density, which in the anelastic approximation is a function of the vertical coordinate only (Lipps & Hemler 1982); π' is the density normalized pressure perturbation, p'/ρ_r;

$\boldsymbol{g} = -g\hat{z}$ is the gravity acceleration adjusted to fit the solar gravity profile, and Θ is the potential temperature defined as $\Theta = T(P_b/P)^{R/c_p}$, where T is the temperature, P is the pressure, P_b is the pressure at the bottom of the domain, R is the universal gas constant, and c_p is the specific heat at constant pressure. The potential temperature is equivalent to the specific entropy through the relation $ds = c_p d(\ln \Theta)$. The subscripts r and a refer to the reference and ambient states, and the superscript $'$ means perturbations of a quantity around the ambient profile. Perturbations of potential temperature are related to perturbations of temperature by the anelastic approximation to the equation of state, $T' = \Theta' T_a/\Theta_a$. The energy equation contains a term forcing the adiabatic perturbations about the ambient state and a thermal relaxation term that damps these perturbations in an inverse timescale $\alpha = \tau^{-1}$. In this setup, while the forcing term tries to mix the fluid in the convection zone, the thermal relaxation keeps the convective unstable state in this layer (see Cossette et al. 2017, for a comprehensive analysis of these effects).

The ambient state defining the thermodynamic variables, ρ_a, Θ_a, and T_a in Equations (1)–(3) is a particular solution of the hydrodynamic equations. In this work we construct the ambient state considering hydrostatic equilibrium as follows:

$$\frac{\partial T_a}{\partial z} = -\frac{g}{R(m+1)}, \tag{4}$$

$$\frac{\partial \rho_a}{\partial z} = -\frac{\rho}{T_a}\left(\frac{g}{R} + \frac{\partial T_a}{\partial z}\right), \tag{5}$$

where $m = m(z)$ is the polytropic index. Solutions of Equations (4) and (5) with $m \geqslant 1.5$ correspond to stable stratification, while solutions for $m < 1.5$ correspond to convectively unstable states.

We use an ambient state with a stable layer at the bottom of the domain by setting $m_s = 2.5$ for $z \leqslant 0.28 L_z$, and a marginally unstable convection zone with $m_u = 1.499991$ for $z > 0.28 L_z$. This is achieved by considering a radial profile of the polytropic index,

$$m(z) = m_s - \frac{1}{2}(m_s - m_u)\left[1 + \text{erf}\left(\frac{z - z_1}{w}\right)\right], \tag{6}$$

where the transition between zones of different m is made through the error functions with $z_1 = 0.28 L_z$ and $w = 0.041 L_z$. Equations (4) and (5) are integrated numerically with $\rho_{z_1} = 208$ kg m^{-3} and $T_{z_1} = 2.322 \times 10^6$ K at the interface between the stable and the unstable layers, $R = 13.732 \times 10^3$ J K^{-1} kg^{-1} is the gas constant for a monoatomic hydrogen gas, and $c_p = 2.5R$. The pressure is computed via the ideal gas equation of state, $P_a = R\rho_a T_a$. The resulting vertical profile of Θ_a is shown in Figure 1(a). In the convective zone, the slope of Θ_a is slightly negative with respect to the z coordinate as can be seen in the figure insert. The negative slope of Θ_a ensures that this zone is unstable to convection, with the difference in Θ_a between the bottom and top of the convectively unstable layer being 18 K. The reference potential temperature $\Theta_r = T_{z_1}$. Finally, for all the simulations, we have considered $\alpha = 1/\tau = 1.29 \times 10^{-8}$ s^{-1}.

The stable zone at the bottom of the domain ensures a more realistic transition between the two layers, allowing a certain

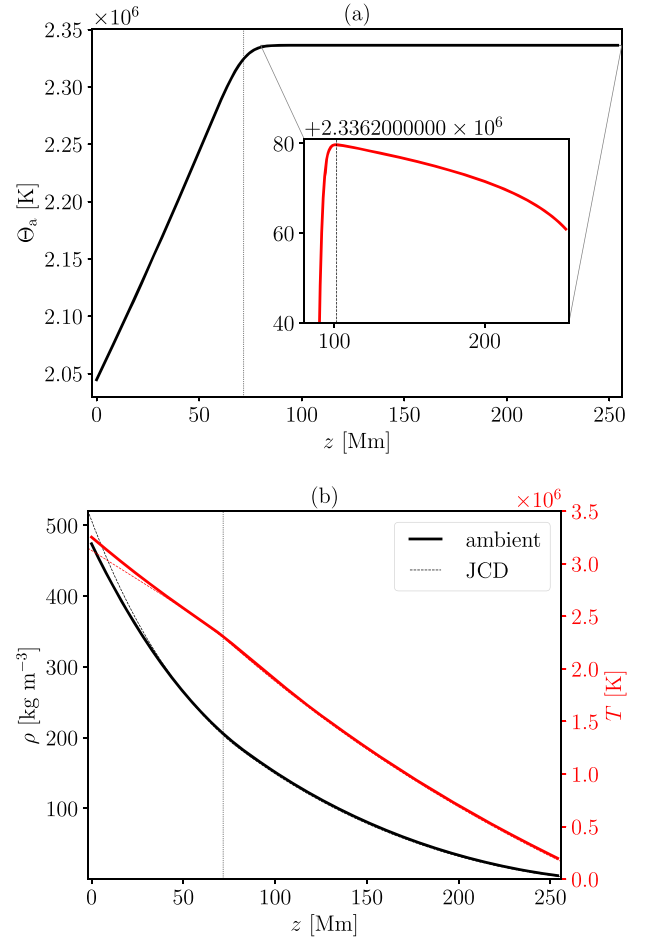**Figure 1.** (a) Vertical profile of the ambient potential temperature, Θ_a. The insert shows a close-up for $0.1L_z < z < L_z$. (b) Vertical profiles of the ambient density (black line) and temperature (red line). The dotted lines correspond to the solar structure model of Christensen-Dalsgaard et al. (1996).

amount of overshooting. This closely resembles situations in nature where convection happens in contact with a stable but not totally rigid layer. As we show below, the dynamics in this stable layer is governed by internal gravity waves (GWs), which induce horizontal motions and react back on the convection properties. Figure 1(b) shows the vertical profiles of the density, ρ_a, and the temperature, T_a. The domain encompasses 4.5 density scale heights.

The boundary conditions for this setup are defined as follows. In the horizontal direction, we consider periodic boundaries for all variables. In the vertical direction, stress-free and rigid boundary conditions for the velocity field are considered, respectively, at the bottom and top of the domain. Null convective radial flux is considered as thermal boundaries at the bottom and top as it has been used in previous works in the literature (e.g., Fan et al. 2003; Hotta et al. 2015). The initial conditions are white noise correlated perturbations in both, u_z and Θ', introduced only in the unstable layer and with amplitudes 5×10^{-4} m s^{-1} and 5×10^{-4} K, respectively. In the next section, we explore the properties of physical quantities (in the real and spectral space) resulting from the simulations with the setup described above but for different resolutions, namely, $N = 64, 128, 256, 512, 768, 1024$, and 2048 cells in each direction. All the simulations were run for at
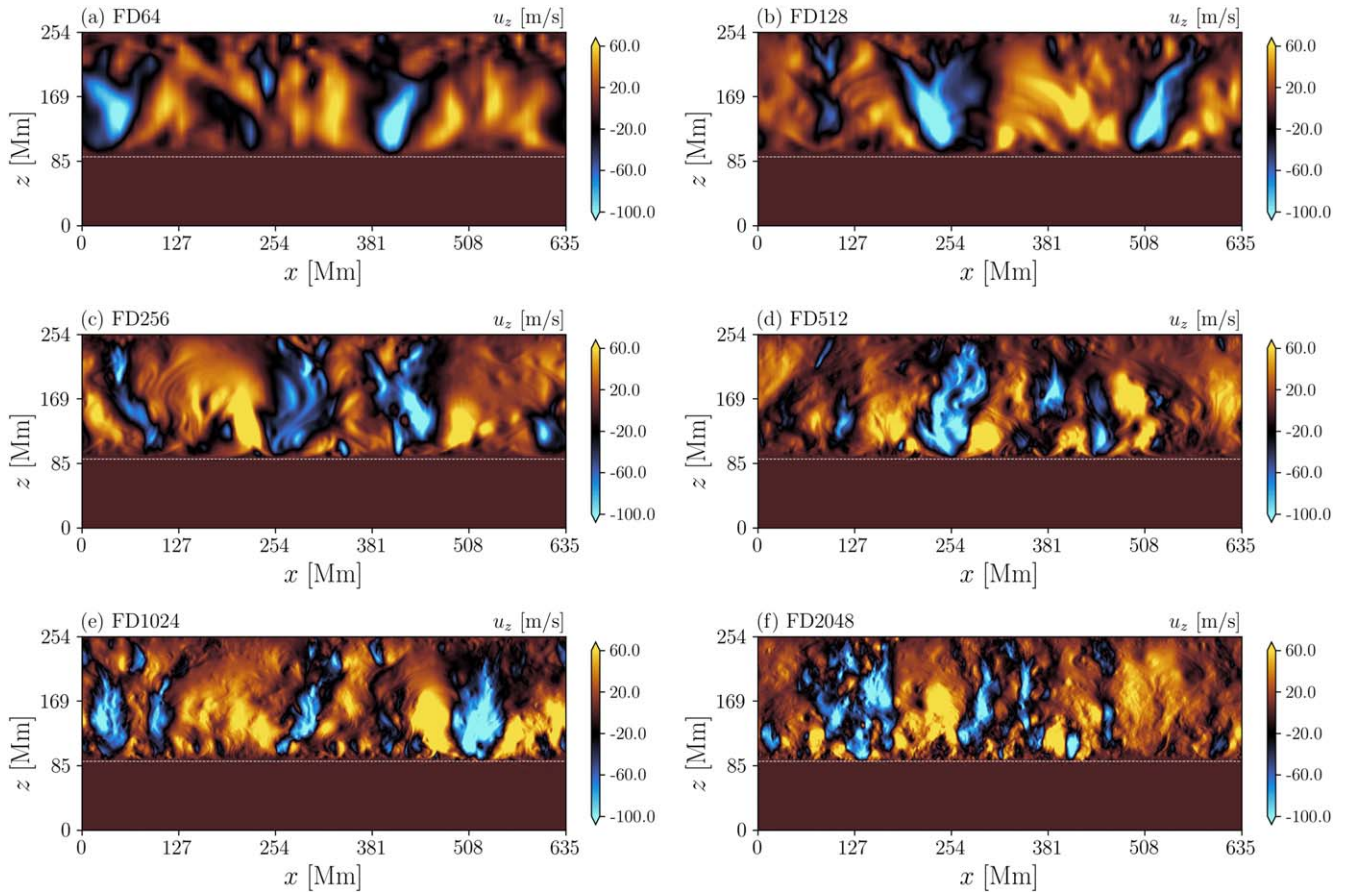
Figure 2. Snapshots of vertical velocity for simulations (a) FD64 to (f) FD2048. Yellow (blue) colors correspond to upflows (downflows). The label of each simulation is shown on the top of each image. An animation of panels (b) and (e) is available. The animation shows, respectively, 2 yr and 5.1 yr of evolution of the vertical velocity for the simulations FD128 (top) and FD1024 (bottom). The real-time duration of the animation is 147 s.

(An animation of this figure is available.)

Table 1
Simulation Parameters and Results

Simulation	N	$\langle u_{rms} \rangle$ (m s^{-1})	$\overline{\nu}_{eff}$ ($\times 10^9$ m^2 s^{-1})	Re$_{eff}$	ℓ (Mm)	ν_t ($\times 10^9$ m s^{-2})
FD64	64	34.0	9.8983	0.7174	42.7	0.484
FD128	128	37.5	0.9820	7.9923	46.5	0.583
FD256	256	40.4	0.0764	110.56	48.2	0.651
FD512	512	41.9	0.0115	758.77	52.3	0.732
FD1024	1024	43.5	0.0033	2698.7	51.8	0.754
FD2048	2048	43.8	0.0013	6933.6	51.2	0.749

Note. Results of simulations with different resolutions, N. In $\langle u_{rms} \rangle$ the velocity is averaged in space and time. The effective viscosity, $\overline{\nu}_{eff}$ is the average over the largest wavenumbers, k. The effective Reynolds number is Re$_{eff} = \langle u_{rms} \rangle L / \overline{\nu}_{eff}$. The convective correlation length, ℓ, is calculated from averages of the kinetic energy spectra at different times according to Equation (15). Finally, $\langle u_{rms} \rangle$ and ℓ are used to compute the turbulent viscosity, ν_t, following Equation (16). The spatial averages were calculated for the convectively unstable layer only ($0.3L_z < z < L_z$).

least 60 yr. This time is sufficient for the simulations to reach a statistically steady state, and to provide enough data for the analysis. The parameters and results of the simulations are summarized in Table 1.

3. Results

3.1. Analysis in Physical Space

Figure 2 shows snapshots of the vertical velocity for simulation from (a) FD64 to (f) FD2048. The yellow and blue contours represent upflows and downflows, respectively. The

canonical picture of convection in the environment with a unstably stratified density profile describes broad upflows and narrow downflows. The figure shows that this feature is well captured by the 2D convection model for low and high resolutions, forming two or three large convective cells. Unlike previous ILES results (Porter & Woodward 1994), in the higher resolution simulations ($N \geqslant 512$), these large cells are not broken by the small-scale structures but coexist with them. The strong downflows seem to be formed by the coalescence of thinner plumes observed at the upper part of the domain.
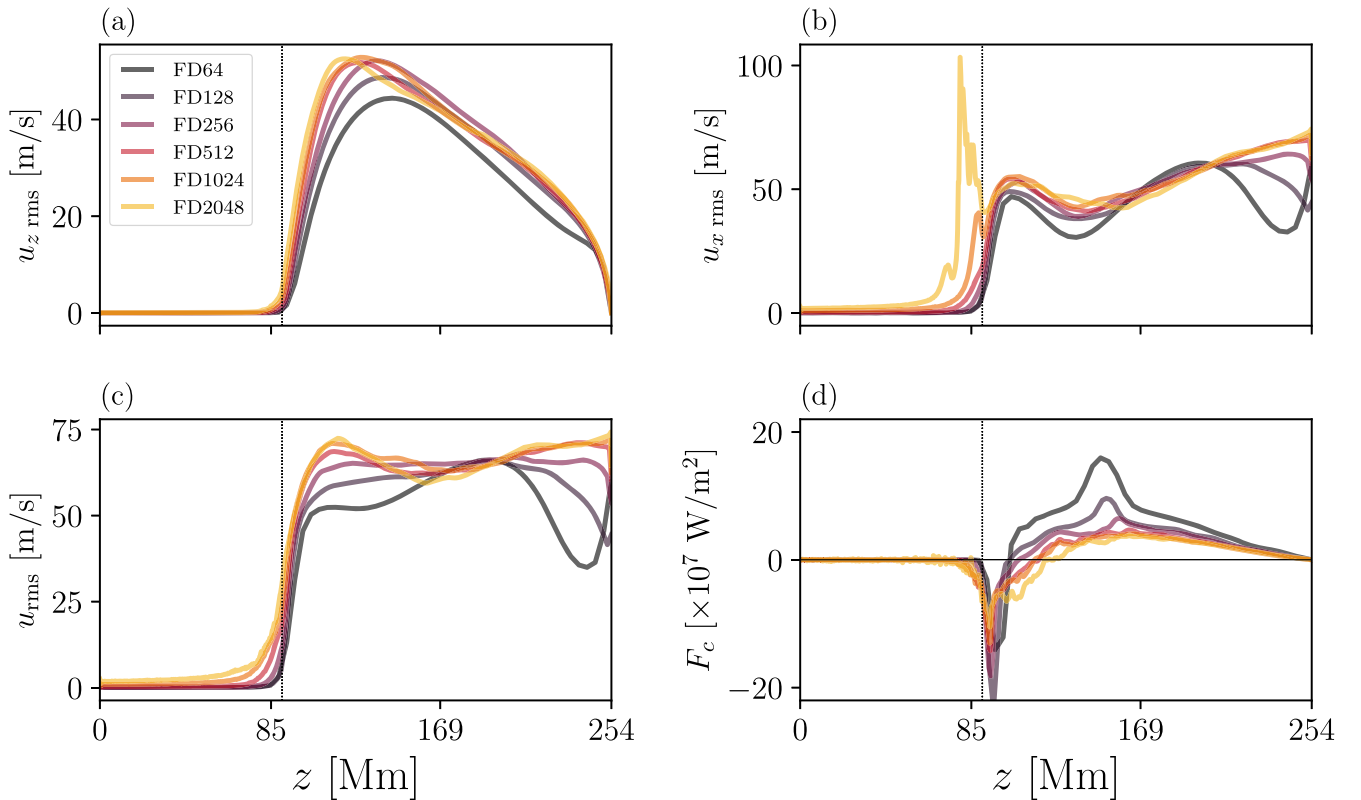
Figure 3. Vertical profiles of the (a) vertical; (b) horizontal; (c) total rms velocities; and (d) the convective heat flux, $F_c = \rho_a c_p \langle u_z \Theta' \rangle$ for simulations FD64–FD2048. Different resolutions are represented by different colors indicated in panel (a).
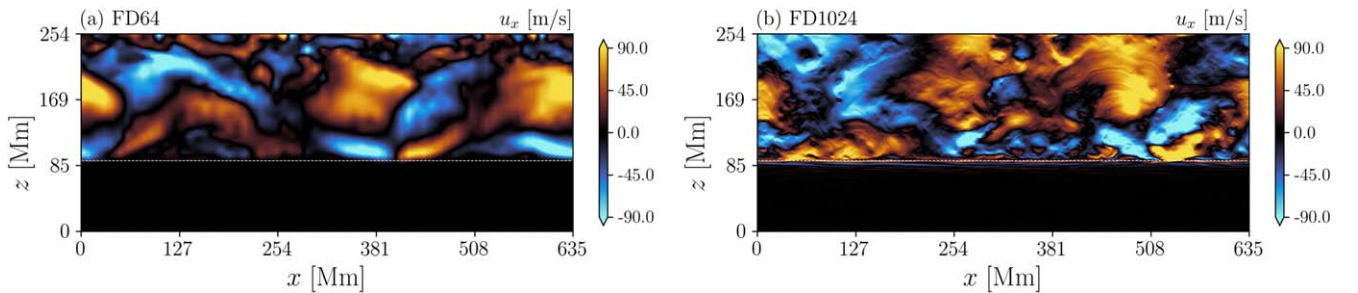

Figure 4. Snapshots of horizontal velocities for simulations (a) FD64 and (b) FD1024. Yellow (blue) contours indicate horizontal flow toward the right (left).

Figure 3 shows $u_{z\,\mathrm{rms}}$ (a), $u_{x\,\mathrm{rms}}$ (b), $u_{\mathrm{rms}} = \sqrt{u_x^2 + u_z^2}$ (c), and the convective flux, $F_c = c_p \rho_r \langle \Theta' u_z \rangle$ (d) as a function of the vertical coordinate z. The rms profiles correspond to averages over the horizontal direction and time during the last 15 yr of the simulations. The profiles of panel (a) are consistent with similar simulations presented in the literature for 2D simulations (Hotta et al. 2012), i.e., the vertical velocity has a peak close to the bottom of the domain. In 3D simulations, compatible to the ones presented here, this maximum is shifted toward the top (e.g., Chan & Sofia 1986; Fan et al. 2003; Hotta et al. 2012). Except for the amplitude, there is no significant change in this profile for different resolutions, and simulations with $N \geqslant 512$ seem to have reached convergence in the location and the value of the maximum value. The profiles of horizontal velocity exhibit significant variations with resolution. For the low-resolution simulations ($N \leqslant 128$), $u_{x\,\mathrm{rms}}$ has two maxima, at the upper and lower parts of the convective layer, and a minimum at $z \sim 135$ Mm. The maxima correspond to fluid

displacements in the opposite direction of the large eddies, whereas the minimum corresponds to the radius where the reversal takes place. In the lower part of the convection zone, this motion has a smaller vertical extension than in the upper part as a consequence of density stratification. When the resolution increases, the profile of $u_{x\,\mathrm{rms}}$ becomes flattened with less prominent maxima and minima. This can be explained by the small-scale structures developed in higher resolution simulations, see Figure 4(b) corresponding to simulation FD1024 as contrasted to the smooth large eddies observed in the low-resolution simulations, see Figure 4(a) corresponding to simulation FD64. In the upper layers, the shorter density scale heights enforces smaller convective structures. For the simulation with $N = 64$, there are eight or less grid points per density scale height, which is insufficient to resolve small-scale convective motions, resulting in larger convective cells. Thus, the horizontal flows have another reversal, which on average forms a second minimum above $z \sim 250$ Mm (see dark gray line in Figure 3(b) and also the upper part of Figure 4(a)). On
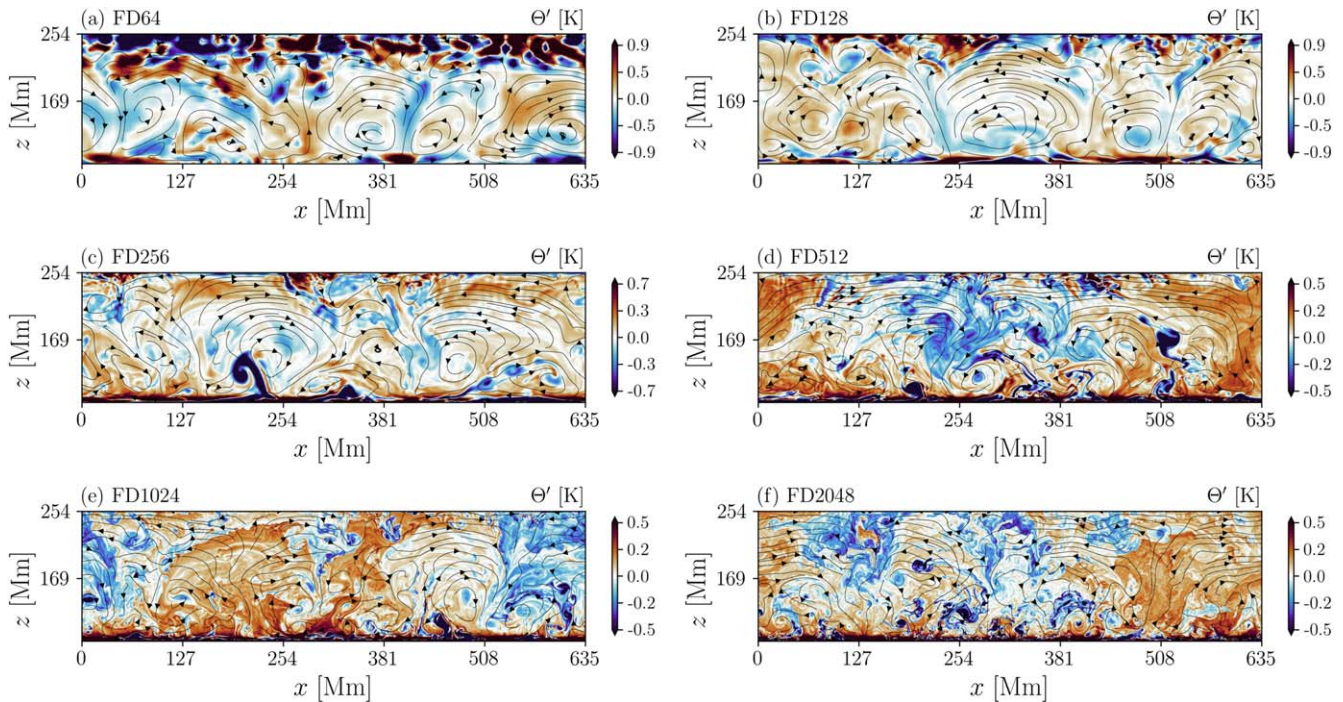
5

Figure 5. Snapshots of perturbations of potential temperature residual, $\Theta' - \langle \Theta' \rangle_z$, for different resolutions. Red contours indicate positive values (hot plumes), blue contours correspond to negative values (cold plumes). The black streamlines show the velocity field with the arrows pointing in the direction of the flow. An animation of panel (e) is available. The animation shows 4.4 yr of evolution of the potential temperature residual for simulation FD1024. The real-time duration of the animation is 83 s.

(An animation of this figure is available.)

the other hand, the simulations with $N > 512$ have at least 32 grid points per density scale height and are able to resolve these structures with the appropriate energy (see, for instance, Figures 2(d)–(f) and 4(b)). After the temporal and horizontal averaging, these cells are wiped out, and the minimum disappears.

Another interesting feature observed in the horizontal velocity is their depth of penetration, which increases with the numerical resolution. Additionally, there is a sharp peak evident in the cases FD1024 and FD2048, which is formed due to generation of internal gravity waves in the stable layer. These waves start to become evident in simulations with $N > 256$ whenever strong downflows induce perturbations in the stable zone (these perturbations are evident in Figure 4(b), after some magnification of the figure, below the white dashed line). However, they are evanescent and dissipate on timescales depending on the numerical resolution. The waves appear to be resolved only in the simulations with 256^2 grid points or greater. For the simulations FD1024 and FD2048, the effective viscosity is so small (see Section 3.3) that the perturbations induced by the gravity waves do not dissipate. Instead, they interfere, and upon a spontaneous symmetry breakdown interact nonlinearly to form mean horizontal flows (Galmiche et al. 2000; Wedi & Smolarkiewicz 2006), evidenced in Figure 3(b) by the peaks with magnitudes that increase with the resolution. For some resolutions these motions create oscillatory patterns; see Section 3.5 for a discussion.

The profiles presented in Figure 3(c) are combinations of the corresponding motions depicted in panels (a) and (b). Their resemblance to the profiles in panel (b) reflects the fact that the horizontal motions are dominant in the convection zone. Finally, the convective heat flux presented in Figure 3(d)

exhibits negative values at the bottom of the convective layer identified with penetrative motions. The higher the resolution, the larger the extent of the overshooting region. On the other hand, the profiles with positive values in the convection zone show that the averaged heat flux carried by convection decreases with N and seems to reach convergent values for $N > 512$.

Figure 5 shows snapshots of the residual of the potential temperature perturbations, $\Theta' - \langle \Theta' \rangle_z$, with the angular brackets meaning vertical average, superimposed with streamlines of the velocity field for all simulations. For a better contrast of the structures we have removed the stable layers from the figures. Note that increasing the resolution allows for progressively more intricate structures in the form of filaments following the edges of convective eddies. These filaments form spikes and swirls due to the fluid movement until they dissolve.

3.2. Analysis in the Fourier Space

To explore further the turbulent characteristics of the convective motions we compute the kinetic power spectrum, $\tilde{E}^K(k, z)$, and the turbulent spectrum of the variance of Θ'. The one-dimensional, temporally averaged, kinetic power spectrum is defined as

$$\tilde{E}^K(k, z) = \frac{1}{2}\tilde{u}(k, z)^*\tilde{u}(k, z), \quad (7)$$

where k is the wavenumber in the x direction, the tilde denotes the Fourier transform of a quantity, and the asterisk denotes complex conjugate. The temporal average is performed considering the last 15 yr of evolution with a sampling rate of 4 months. The power spectrum of the variance of potential
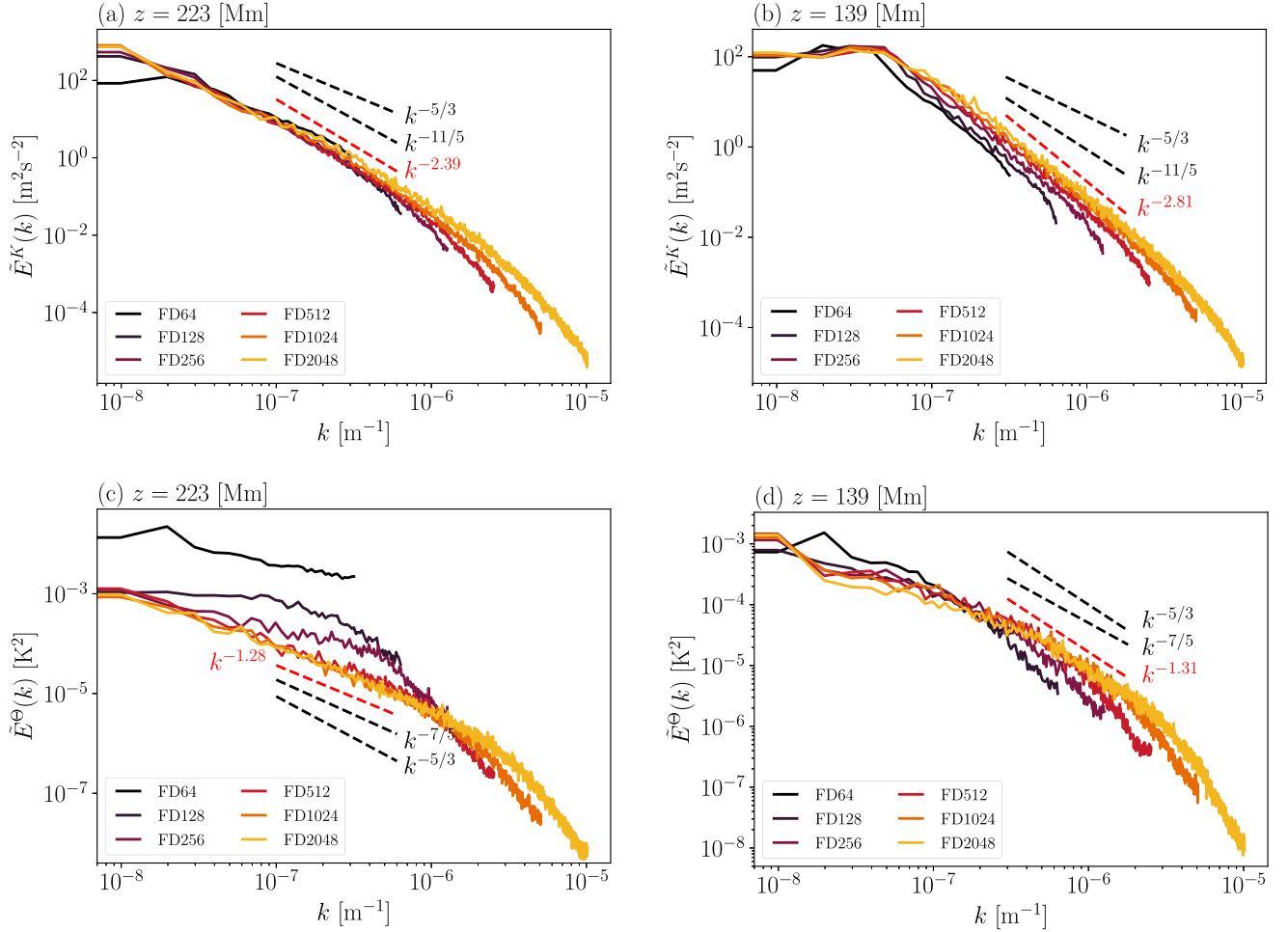
Figure 6. Power spectra of the kinetic energy, upper panels, and the variance of potential temperature, bottom panels, for different numerical resolutions. Panels (a) and (c) correspond to the upper part of the domain, $z = 223$ Mm; and panels (b) and (d) to the middle of the convection zone, $z = 139$ Mm. The black dashed lines are guides to the KO and BO scaling laws, and the red dashed lines correspond to the adjusted scaling for simulation FC1024 in the inertial range.

temperature, $\tilde{E}^\Theta(k, z)$, is defined analogously by replacing $\tilde{u}(k, z)$ by $\tilde{\Theta}'(k, z)$ in Equation (7). Since we expect the properties of convection to depend on the height, we perform this computation for the top and the middle of the convection zone, $z = 223$ and 139 Mm, respectively.

A comparison of the kinetic power spectrum of simulations with different resolutions is presented in Figure 6 for $z = 223$ Mm (a) and $z = 139$ Mm (b) as a function of the wavenumber; panels (c) and (d) display the power spectrum of the variance of potential temperature, $\tilde{E}^\Theta(k, z)$ for the same heights.

In 3D isotropic turbulence, $\tilde{E}^K(k)$ and $\tilde{E}^{\Theta'}(k)$ scale according to the Kolmogorov law, as $k^{-5/3}$ (Kolmogorov 1941; Obukhov 1959, hereafter KO scaling). In the presence of the buoyancy force, but still for isotropic motions, the scaling should be $\tilde{E}^K(k) \sim k^{-11/5}$ and $\tilde{E}^{\Theta'}(k) \sim k^{-7/5}$ (Bolgiano 1959; Obukhov 1959, hereafter the BO scaling). Our simulations are in 2D and the motions are clearly anisotropic as can be observed in Figure 2. Therefore, none of the scaling laws above should be applicable. Nonetheless, for the sake of comparison the black dashed lines in Figure 6 compare these scaling laws with the scaling found for the inertial range in our simulation with $N = 1024$ (in red). At both heights the kinetic and thermal spectra are closer to the BO than to the KO scaling laws.

It is noticeable that the kinetic spectra at the upper levels of the convection zone, panel (a) have inertial range starting at almost the largest scales, whereas in the middle of the convection zone, panel (b), the inertial range starts at $k \sim 10^{-7}$ m^{-1}. As expected, the inertial range extends over more wavenumbers as the resolution increases, reaching the dissipative Kolmogorov scale at the smallest resolved scales. The scaling law of the energy in the inertial range changes from one depth to the other. This change might be a manifestation of differences in the anisotropy of convective motions at different depths. Except for the simulation FD64, there is a good agreement between results of different simulations in the kinetic power in most of the inertial range at $z = 223$ Mm and at the large scales, $k \lesssim 10^{-7}$ m^{-1}, for $z = 139$ Mm. Our results are in contrast to the DNS simulations performed by Featherstone & Hindman (2016), where the large scales lose energy when the dissipative coefficients are diminished and smaller scales are resolved. However, there is an agreement between our findings, i.e., convergence of the spectra for the large scales, and the results of the LES simulations of Sullivan & Patton (2011). This suggests that subgrid scale (SGS) or implicit SGS methods properly capture the inverse energy cascade from the smaller to the larger scales.

The profiles of $\tilde{E}^{\Theta'}(k)$ in Figure 6(c) present evidence of the lack of resolution discussed above in simulations FC64–FC256
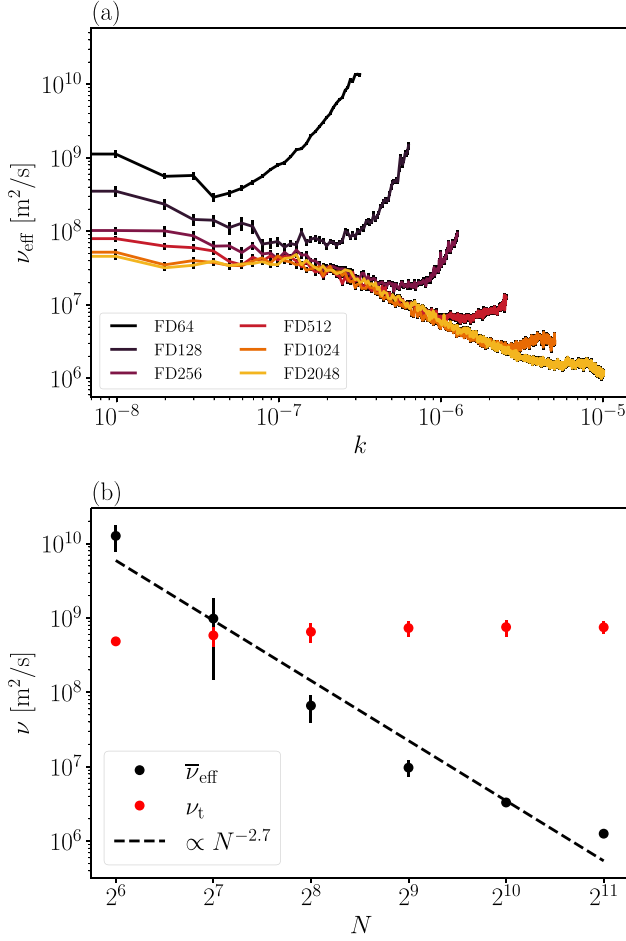
Figure 7. (a) Effective numerical viscosity as a function of the wavenumber, k, for simulations with different resolutions; (b) effective numerical viscosity (black points) of the smallest resolved scales and turbulent viscosity (red) vs. the resolution, N. Upper and bottom panels show vertical error bars multiplied by a factors of 2 and 10, respectively, to make them noticeable. The black dashed line shows a fitted power law as indicated in the legend.

3.3. Numerical Viscosity

We estimate the effective viscosity, $\nu_{\rm eff}$, for the simulations with all the tested resolutions. There are several techniques to conduct this calculation for ILES simulations, most of them performed with the physical quantities represented in the Fourier space (e.g., Zhou et al. 2014), but some methods also perform this computation in both physical and spectral spaces (Schranner et al. 2015). Domaradzki et al. (2003) presented a method to compute the numerical viscosity for an EULAG simulation of decaying turbulence. Here, we adapt the method implemented by Domaradzki et al. (2003) and developed later for convection simulations in spherical coordinates by Strugarek et al. (2016) to our Cartesian 2D simulations.

Besides providing the profile of $\nu_{\rm eff}$ as a function of the wavenumbers for each resolution, i.e., the amount of viscosity for different scales, the method allows a clear comparison of this quantity as the numerical resolution varies.

To estimate the effective viscosity we Fourier transform all terms in Equation (2), and take the dot product on both sides with $\rho_r \boldsymbol{u}_k^*$, where $\boldsymbol{u}_k = \boldsymbol{u}(t, k, z)$. Then, we average the resulting equation with respect to t and z, and add the contribution of the effective viscosity to obtain the following equation:

$$\frac{\partial \varepsilon_k}{\partial t} = \mathcal{A}_k + \mathcal{P}_k + \mathcal{G}_k + \mathcal{D}_k(\nu_{\rm eff}), \qquad (8)$$

where the kinetic density energy term is given by

$$\varepsilon_k = \frac{1}{2} \langle \rho \boldsymbol{u}_k \cdot \boldsymbol{u}_k^* \rangle, \qquad (9)$$

while the terms corresponding to advection, pressure, gravitational potential energy, and the effective viscous dissipation rates are, respectively, given by

$$\mathcal{A}_k = -\langle \rho_r [(\boldsymbol{u} \cdot \nabla)\boldsymbol{u}]_k \cdot \boldsymbol{u}_k^* \rangle, \qquad (10)$$

$$\mathcal{P}_k = -\langle \rho_r (\nabla \pi')_k \cdot \boldsymbol{u}_k^* \rangle, \qquad (11)$$

$$\mathcal{G}_k = -\left\langle \rho_r \boldsymbol{g} \left(\frac{\Theta'}{\Theta_r}\right)_k \cdot \boldsymbol{u}_k^* \right\rangle, \qquad (12)$$

and

$$\mathcal{D}_k(\nu) = \left\langle \left\{ \frac{\partial}{\partial x_j} \left[2\rho_r \nu \left(e - \frac{1}{3}\delta_{ij} \nabla \cdot \boldsymbol{u} \right) \right] \hat{\boldsymbol{e}}_i \right\}_k \cdot \boldsymbol{u}_k^* \right\rangle, \quad (13)$$

where $\langle \cdot \rangle$ means the average over z and time.

If the averages are taken during the statistically steady state and over a long period of time, the left-hand side of Equation (8) is approximately zero. Thus, dividing the remaining equation by $-\mathcal{D}_k(\nu = 1)$, reorganizing and overlooking the fact that $\nu_{\rm eff}$ might be dependent on the space coordinates, we obtain an estimate of the effective viscosity of the system,

$$\frac{\mathcal{A}_k + \mathcal{P}_k + \mathcal{G}_k}{-\mathcal{D}_k(\nu = 1)} = \frac{-\mathcal{D}_k(\nu = \nu_{\rm eff})}{-\mathcal{D}_k(\nu = 1)} = \nu_{\rm eff}(k). \qquad (14)$$

The reader should be aware of the several approximations made to compute what we call numerical or effective viscosity throughout this paper. In ILES the SGS viscosity is nonlinear, intermittent in space and time. On the other hand, our estimate for this contribution, $\nu_{\rm eff}$, is considered constant with the depth and results from spatial and temporal averages. Furthermore, in the MPDATA algorithm implemented in the EULAG-MHD code, besides the dissipative terms, there are dispersive SGS contributions, effectively responsible for inverse cascades (Margolin & Rider 2002). These terms are evidently not captured by Equation (13). Therefore, $\nu_{\rm eff}$ is an integral measure of the SGS viscosity, which also embodies other SGS contributions implicit in the numerical technique.

In Figure 7(a), we present $\nu_{\rm eff}(k)$ for the simulations with different resolutions. For the large scales, $k < 10^{-7}$ m^{-1}, $\nu_{\rm eff}$ decreases from 10^9 m^2 s^{-1} to 6×10^7 m^2 s^{-1}. The difference in $\nu_{\rm eff}$ between the different simulations decreases as the resolution increases. For simulations FD64–FD256, the profiles of $\nu_{\rm eff}$ have a minimum for the intermediate scales and an increase for the smallest scales. Qualitatively, these profiles

at the upper layers of the domain where the density scale height is small. It is manifested in excess of energy at all scales for FC64 and at intermediate scales for FC128 and FC256. On the other hand, simulations FC512–FC2048 show convergence in the inertial range of the power spectra. In the middle of the convection zone, where the density scale height is larger, most of the simulations have similar power spectra, differing only in the extent of the inertial range (see panel (d)).

resemble the results of Domaradzki et al. (2003). The profiles obtained by Strugarek et al. (2016) for a global simulation with $51 \times 64 \times 128$ grid points also show increasing effective viscosity for large wavenumbers. However, in their more sophisticated three-dimensional procedure they obtain large errors for the low wavenumbers and do not consider the results for these scales. A comparison of the values of ν_{eff} averaged over large wavenumbers shows quantitative agreement between the results of Strugarek et al. (2016, 2018) and our simulations FD128 and FD256. The results of Strugarek et al. (2018) show that the effective viscosity depends on the strength of convection, the density contrast, and/or rotation. Yet, this dependency is weak when compared to the changes found here for different resolutions.

For the cases FD256–FD2048, there is an intermediate range of k, for which ν_{eff} is the same for all resolutions. For the smallest scales, it has decreasing values with the increase of the numerical resolution. For FD512–FD2048, the profile of ν_{eff} does not increase but remains roughly constant. Figure 7(a) shows error bars for this estimation multiplied by 2 to make them distinguishable. The error is computed as $\sigma/\sqrt{n}$, where σ is the standard deviation of the temporal average and n is the number of temporal samples used in the computation corresponding to the last 15 yr of the simulations. Thus, n is of the order of 50, for the considered sampling times.

The magnitude of the effective viscosity averaged over the largest wavenumbers resolved for each simulation, i.e., over the Kolmogorov scales, is presented in Table 1 and depicted in Figure 7(b) as a function of N. It decreases as the resolution increases following a power law, $\overline{\nu}_{\mathrm{eff}} \propto N^{\alpha}$, with exponent $\alpha = -2.7$. However, the power is higher for the low-resolution cases and smaller for simulations with $N > 512$. With the value of $\overline{\nu}_{\mathrm{eff}}$ and u_{rms} (see Table 1) we can compute an effective Reynolds number, $\mathrm{Re}_{\mathrm{eff}} = u_{\mathrm{rms}} L/\overline{\nu}_{\mathrm{eff}}$ (with $L = 0.3 R_{\odot}$, i.e., the size of the convection zone), reached by the simulations. Its values go from ~ 1 to $\sim 7 \times 10^{3}$, and its variation as a function of N, presented in Figure 8, follows a power law $\mathrm{Re}_{\mathrm{eff}} \propto N^{2.7}$.

3.4. Turbulent Viscosity

Even though the effective viscosity decreases with the resolution following a power law, Figures 3 and 6 evidence convergence of the simulation results. This implies that, despite the smallest values of ν_{eff} in the high-resolution cases, the dynamics of the system is governed by an enhanced dissipation, likely provided by turbulence, which efficiently transports momentum and heat. The turbulent viscosity, ν_{t}, depends on the time and spatial scales of the most energetic eddies, which are model-dependent quantities. They are sensitive to variations in the domain's aspect ratio, the ambient state and the timescale of the thermal relaxation (Cossette & Rast 2016). In this section, we determine ν_{t} to verify if it also depends on the resolution and how its values compare with those of ν_{eff}.

To do so, we calculate first the turbulent correlation length of the convective motions using (Pope 2011),

$$\ell = \frac{\int \tilde{E}(k)/k\, dk}{\int \tilde{E}(k)\, dk}. \tag{15}$$

Equation (15) can be seen as a weighted average of the inverse of the wavenumbers, where the weights are given by the kinetic energy. Therefore, it provides the typical length of
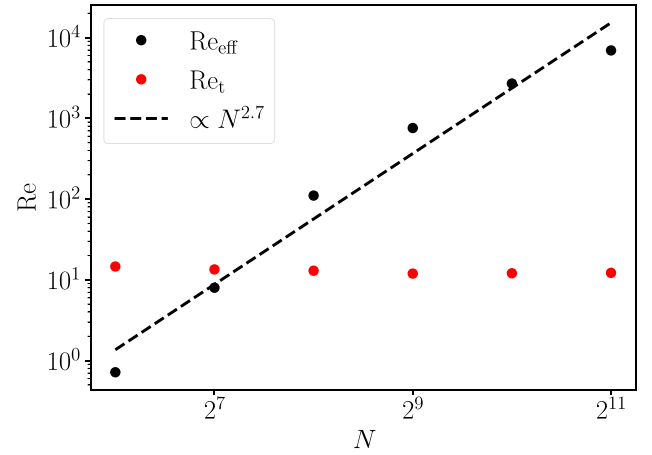

Figure 8. Effective Reynolds number (black points) and turbulent Reynolds (red) number as a function of the resolution. The black dashed line shows a fitted power law as indicated in the legend.

the most energetic convective eddies. Their values vary between ~ 40 and ~ 50 Mm as presented in Table 1.

With the correlation length, ℓ, we estimate the turbulent viscosity as (see, e.g., Kitchatinov et al. 1994)

$$\nu_{\mathrm{t}} = \frac{1}{3}\ell u_{\mathrm{rms}}. \tag{16}$$

The values of ν_{t} as a function of N are presented as red points in Figure 7(b). They slightly rise as the resolution increases from $\sim 5 \times 10^{8}$ to $\sim 8 \times 10^{8}$ m^{2} s^{-1}. These values have the same order of magnitude of recent estimations of the turbulent magnetic diffusivity due to granulation and supergranulation in the solar surface (Skokić et al. 2019), which suggest that our model parameters are in an appropriate regime.

The variance of ν_{t} for different resolutions is rather small when compared to the changes of $\overline{\nu}_{\mathrm{eff}}$ which span about 4 orders of magnitude. As a consequence, the Reynolds number computed from the turbulent viscosity remains roughly constant with values ~ 13 while the effective Reynolds number increases 4 orders of magnitude, see Figure 8. From Figure 7(b), it can be seen that only the simulation FD64 has effective viscosity considerably larger than the turbulent one. For all the other cases, $\nu_{\mathrm{t}} > \overline{\nu}_{\mathrm{eff}}$ implies that the system is governed by the large scales. The relevant question is, why do these scales, especially in the bulk of the convection zone, have similar spatiotemporal correlations regardless of the resolution? The results presented in Sections 3.1–3.3 indicate convergence for simulations FD512–FD2048 with well-resolved dynamics. For simulations FD128 and FD256, the agreement is not perfect, but the large scales behave alike. This might be a consequence of the implicit SGS contribution toward the dynamically dominant scales. The different profiles of $\nu_{\mathrm{eff}}(k)$ between these two sets of simulations provide some support to this hypothesis; note the increasing values of ν_{eff} for the smallest scales in models with $N = 128, 256$.

3.5. Internal Gravity Waves and Mean Flows in the Stable Layer

As a consequence of convective overshooting, internal gravity waves are excited and propagate in the stable layer.
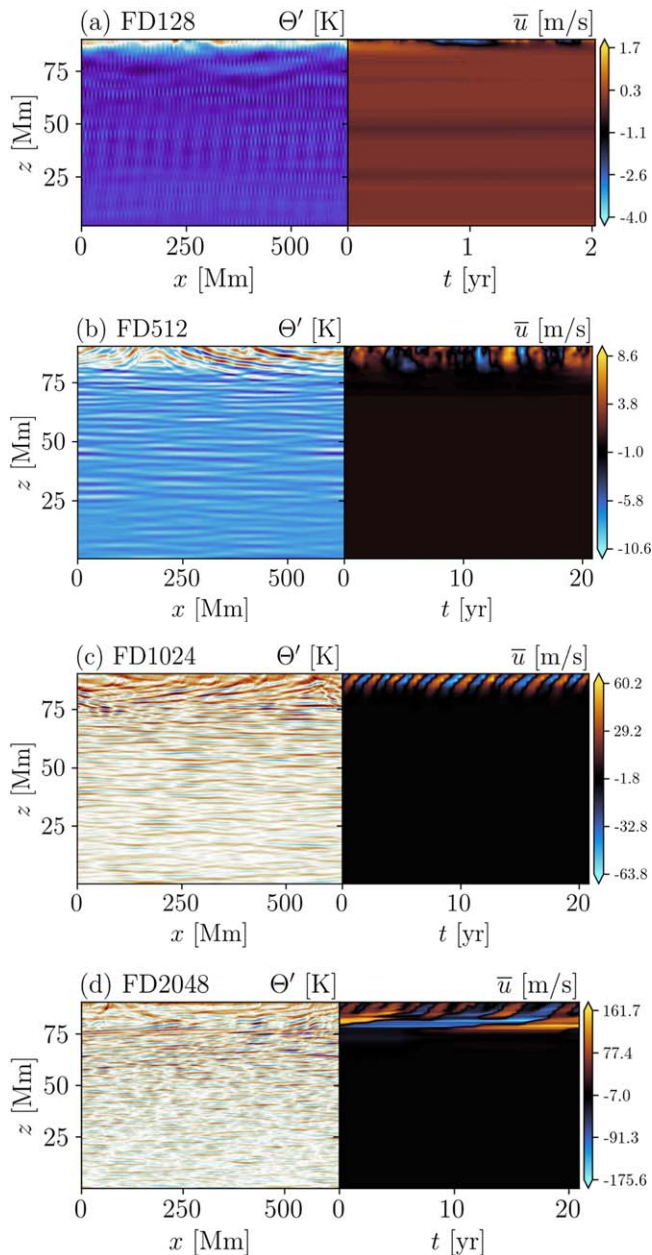
Figure 9. Left panels: snapshots of Θ' for simulations (a) FD128, (b) FD256, (c) FD1024, and (d) FD2048. The aspect ratio of this panel is modified for visualization purposes. Right panels: propagation in the plane (t, z) of the velocity component, u, averaged over the horizontal direction, x. The time corresponds to the last 20 yr of evolution during steady state.

Interestingly, together with these waves a mean horizontal motion develops in the stable layer. In our high-resolution experiments this motion reverses sign periodically as can been seen in Figure 9. The left panels show snapshots of Θ' in the stable layer. The gravity waves are unresolved in the simulation FD128, barely captured in FD512, and resolved in FD1024 and FD2048. The right panels show the temporal evolution of $\bar{u}$, where the overline represents average over the horizontal direction, during the last 20 yr of the simulated time. For the case FD128, there is an unorganized, low amplitude pattern at the very upper fraction of the stable interior. For FD512, the mean flow is more evident showing nonperiodic reversals. For FD1024, a well-organized pattern of mean flow reversing sign every ~ 1 yr emerges. The amplitude of this flow reaches

60 m s^{-1}, which is of the same order of the horizontal motions in the convection zone. Finally, because of a small viscosity, for FD2048, these motions have large amplitudes, change direction in a random form, and persist for longer time at $z \sim$ 75 Mm forming two or three layers of mean flow, $\bar{u}$, at the same time. Similar results were discussed for small viscosity simulations in Wedi & Smolarkiewicz (2006). These motions are reminiscent of the Earth quasi-biennial oscillation (Baldwin et al. 2001), which are a consequence of interacting gravity waves and depend on the kinematic viscosity of the medium (Lindzen & Holton 1968; Holton & Lindzen 1972; Plumb & McEwan 1978; Kim & MacGregor 2001; Wedi & Smolarkiewicz 2006). If existing inside the solar radiative zone, they may be relevant for the transfer of angular momentum and may interact with large-scale motions in the convection zone, likely contributing to the formation of torsional patterns. Since the goal of this work is exploring the role of numerical resolution, we postpone a more detailed physical discussion on the physics of GW and these mean flows for future works.

4. Conclusions

Direct numerical simulations of natural systems at high Reynolds numbers are unattainable for present supercomputers. Fortunately, the LES and ILES methods provide capabilities of reproducing turbulent flows. However, for systems with scarce observational constraints, such as stellar convection zones, determining whether LES or ILES capture the system's physics is a challenging task.

The aim of this paper was to address this problem by exploring the numerical convergence in ILES simulations of turbulent convection in two dimensions. The model is constructed over the anelastic set of equations solved by the EULAG-MHD code. It considers an atmosphere with characteristics of the solar interior, including a fraction of the radiative zone and the convection zone. The simulations were performed with resolution increasing from 64^2 up to 2048^2 grid points. The results present the values of the effective and turbulent viscosities and other integral characteristics of the numerical solutions. Another goal was to observe how the large scales behave when interacting with the progressively smaller resolved scales.

Spatial and temporal averages demonstrate that quantities such as the rms velocities have similar vertical profiles for resolutions even as coarse as $N \sim 128$. We noticed that the structure of the flow, characterized by narrow downdrafts and broad upflows crossing the entire convective layer of the model, is conserved even when these motions interact with the smallest structures (Figures 2 and 5). This result stands in contrast to the results of 2D ILES of Porter & Woodward (1994) where the progressive development of small scales leads to the destruction of the large structures. This difference might arise from the differences between PPM and MPDATA ILES formulations, but mostly from the compressible character of their simulations, which imposes structural changes in the temperature and density profiles as the effective viscosity decreases. These changes result in different convective models for each resolution.

As for the spectral behavior, we notice that for resolutions with $N \gtrsim 128$, the kinetic energy spectra are similar at the middle and the top of the convection zone, whereas the length of the inertial range increases with N reaching more than two

decades for our highest resolution model. As for the turbulent spectrum of the variance of Θ', in the top, it reflects the lack of resolution of the FD64–FD256 simulations due to the small density scale height. Convergence is observed, however, in simulations with $N \geqslant 512$. In the middle of the convection zone, simulations with $N = 128$ or more grid points agree in the injection and inertial ranges.

A deeper analysis of the energy balance in the Fourier space allows us to estimate the effective viscosity of the simulations as a function of the wavenumber. For the large scales, the profiles of ν_{eff} in all the simulations are slightly decreasing with k, and with magnitudes progressively decreasing with N. For $N \geqslant 256$, there is a range of intermediate scales where the values and profiles of ν_{eff} closely match. These profiles separate for the smallest resolved scales. For the smallest scales, the profiles of ν_{eff} increase with k for resolutions with $N \leqslant 256$, but remain roughly constant for $N \geqslant 512$. Our interpretation of this change has to do with the simplified assumptions made for the residual of the balanced Equation (2) in the steady state. We assumed that the residual corresponds only to an effective viscosity depending on the scale but constant in time. However, in MPDATA the numerical formulation contains dissipative as well as dispersive terms, both intermittent in time and space. The contribution of the dispersive terms is mediating the transfer of energy between scales. Thus, the increasing of ν_{eff} for the smaller scales in the low-resolution cases can be related to the enhanced SGS contribution of the numerical algorithm. Yet, the small-scale contribution is thoroughly resolved at higher resolutions. Therefore, the profile of ν_{eff} would incorporate only viscous dissipation.

Averaging $\nu_{\mathrm{eff}}(k)$ over the dissipative, Kolmogorov, scales shows a power-law relation between the effective viscosity and the resolution, $\overline{\nu}_{\mathrm{eff}} \propto N^{-2.7}$. Note, however, that the curve could be fitted by two different power laws for $N \leqslant 256$ and $N \geqslant 512$, which supports our conclusion above on the SGS contributions. With the obtained values of $\overline{\nu}_{\mathrm{eff}}$ the effective Reynolds numbers the simulations span between ~ 1 and $\sim 10^4$. On the other hand, the values of the turbulent eddy viscosity, ν_{t}, are of the order of 10^8 m^2 s^{-1} and are barely dependent of the grid size. Only the simulation FD64 has an average effective viscosity larger than this value. Thus, despite that small-scale structures are sharply resolved in high-resolution cases, the dynamics of the system is determined by the turbulence, which has an eddy Reynolds number of the order of 10. We argue that the diagnostics observed for simulations FD512–FD2048 indicated convergent well-resolved turbulence. The fact that the properties of the large scales in simulations FD128 and FD256 behave like the better resolved ones evidences the SGS contribution of the advection solver MPDATA. The convergent LES simulations of Porter & Woodward (2000) and Sullivan & Patton (2011) obtained results in agreement to the ones outlined here. Alternatively, the DNS simulations of Featherstone & Hindman (2016) indicate that decreasing the dissipation coefficients diminishes the energy of the large scales in benefit of the smallest ones.

Despite the simulations presented here being 2D, the results of this research support the idea that ILES are efficient in capturing the dynamics of turbulent systems. A note of caution is due here for regions where the thermal stratification enforces the formation of small structures not well resolved by the grid as in cases FD64 and FD128. Having a nonhomogeneous grid could be appropriate for these situations. Nevertheless, if the model encompasses both stable and unstable layers, as in our case, high resolution is necessary to capture the dynamics in the stable layer dominated by gravity waves. This is demonstrated in Section 3.5 where mean oscillatory motions emerge only for sufficiently low effective viscosities. A relevant question raised by this study is how much the interaction between these two layers modifies the dynamics of the turbulent convection. Simulations of convection in 3D and/or in different geometries that may help answer this question will be explored in future work.

ORCID iDs

G. Guerrero (ID) https://orcid.org/0000-0002-2671-8796
A. G. Kosovichev (ID) https://orcid.org/0000-0003-0364-4883

References

Baldwin, M. P., Gray, L. J., Dunkerton, T. J., et al. 2001, RvGeo, 39, 179
Bolgiano, R., Jr. 1959, JGR, 64, 2226
Brandenburg, A., Chan, K. L., Nordlund, Å., & Stein, R. F. 2005, AN, 326, 681
Canuto, V. M. 2000, MNRAS, 317, 985
Chan, K. L., & Sofia, S. 1986, ApJ, 307, 222
Christensen-Dalsgaard, J., Dappen, W., Ajukov, S. V., et al. 1996, Sci, 272, 1286
Colella, P., & Woodward, P. R. 1984, JCoPh, 54, 174
Cossette, J.-F., Charbonneau, P., Smolarkiewicz, P. K., & Rast, M. P. 2017, ApJ, 841, 65
Cossette, J.-F., & Rast, M. P. 2016, ApJL, 829, L17
Domaradzki, J. A., Xiao, Z., & Smolarkiewicz, P. K. 2003, PhFl, 15, 3890
Elliott, J. R., & Smolarkiewicz, P. K. 2002, IJNMF, 39, 855
Fan, Y., Abbett, W. P., & Fisher, G. H. 2003, ApJ, 582, 1206
Featherstone, N. A., & Hindman, B. W. 2016, ApJ, 818, 32
Galmiche, M., Thual, O., & Bonneton, P. 2000, DyAtO, 31, 193
Ganot, Y., Dragila, M. I., & Weisbrod, N. 2014, AgFM, 184, 12
Greer, B. J., Hindman, B. W., Featherstone, N. A., & Toomre, J. 2015, ApJL, 803, L17
Guerrero, G., Smolarkiewicz, P. K., de Gouveia Dal Pino, E. M., Kosovichev, A. G., & Mansour, N. N. 2016a, ApJ, 819, 104
Guerrero, G., Smolarkiewicz, P. K., de Gouveia Dal Pino, E. M., Kosovichev, A. G., & Mansour, N. N. 2016b, ApJL, 828, L3
Hanasoge, S., Gizon, L., & Sreenivasan, K. R. 2016, AnRFM, 48, 191
Holton, J. R., & Lindzen, R. S. 1972, JAtS, 29, 1076
Hotta, H., Rempel, M., & Yokoyama, T. 2015, ApJ, 798, 51
Hotta, H., Rempel, M., Yokoyama, T., Iida, Y., & Fan, Y. 2012, A&A, 539, A30
Käpylä, P. J., Viviani, M., Käpylä, M. J., Brandenburg, A., & Spada, F. 2019, GApFD, 113, 149
Kim, E.-j., & MacGregor, K. B. 2001, ApJL, 556, L117
Kitchatinov, L. L., Pipin, V. V., & Ruediger, G. 1994, AN, 315, 157
Kitiashvili, I. N., Kosovichev, A. G., Mansour, N. N., & Wray, A. A. 2016, ApJL, 821, L17
Kolmogorov, A. 1941, DoSSR, 30, 301
Lindzen, R. S., & Holton, J. R. 1968, JAtS, 25, 1095
Lipps, F. B., & Hemler, R. S. 1982, JAtS, 39, 2192
Margolin, L. G., & Rider, W. J. 2002, IJNMF, 39, 821
Obukhov, A. 1959, DoSSR, 125, 1246
Peña-Ortiz, C., Manzini, E., & Giorgetta, M. A. 2019, JCli, 32, 7453
Plumb, R. A., & McEwan, A. D. 1978, JAtS, 35, 1827
Pope, S. B. 2011, Turbulent Flows (Cambridge: Cambridge Univ. Press)
Porter, D. H., & Woodward, P. R. 1994, ApJ, 93, 309
Porter, D. H., & Woodward, P. R. 2000, ApJ, 127, 159

Prusa, J. M., Smolarkiewicz, P. K., & Wyszogrodzki, A. A. 2008, CF, 37, 1193
Sakievich, P., Peet, Y., & Adrian, R. 2016, IJHFF, 61, 183
Schranner, F. S., Domaradzki, J. A., Hickel, S., & Adams, N. A. 2015, CF, 114, 84
Schwarzschild, M. 1959, ApJ, 130, 345
Skokić, I, Brajša, R., Sudar, D., Ruždjak, D., & Saar, S. H. 2019, ApJ, 877, 142
Smolarkiewicz, P. K. 2006, IJNMF, 50, 1123
Smolarkiewicz, P. K., & Charbonneau, P. 2013, JCoPh, 236, 608
Stevens, R. J., Blass, A., Zhu, X., Verzicco, R., & Lohse, D. 2018, PhRvF, 3, 041501

Stothers, R. B. 2000, MNRAS, 314, L7
Strugarek, A., Beaudoin, P., Brun, A. S., et al. 2016, AdSpR, 58, 1538
Strugarek, A., Beaudoin, P., Charbonneau, P., & Brun, A. S. 2018, ApJ, 863, 35
Sullivan, P. P., & Patton, E. G. 2011, JAtS, 68, 2395
Wang, L., Zhou, T., Li, J., et al. 2019, JMetR, 33, 949
Wedi, N. P., & Smolarkiewicz, P. K. 2006, JAtS, 63, 3226
Zhou, Y., Grinstein, F. F., Wachtor, A. J., & Haines, B. M. 2014, PhRvE, 89, 013303